Electronic Supporting Information for

Tuning oxygen-containing microenvironment of Pt-Ni hetero-interface to accelerate alkaline hydrogen oxidation

Jiantao Fu, Wuyi Feng, Xinye Zheng, Yingzheng Zhang, Di Zhao,* Jiatao Zhang

Key Laboratory of Cluster Science, Beijing Key Laboratory of Construction-Tailorable Advanced Functional Materials and Green Applications, School of Chemistry and Chemical Engineering, Beijing Institute of Technology, Beijing 100081, China.

Table of contents

Experimental Section

Chemicals and materials.

The nickel-coated carbon nanotubes (Ni/CNTs) and potassium hydroxide (KOH) were purchased from Macklin Bio-chemical Technology Co., Ltd. Potassium chloride (KCl) and ferric nitrate ($Fe(NO_3)_3$) were purchased from Meryer Chemical Technology Co., Ltd. Chloroplatinic acid (H_2PtCl_6) and ethanol were obtained from Beijing Tongguang Fine Chemical Co., Ltd. Nafion solution (5 wt.%) was purchased from Alfa Aesar Chemical Co., Ltd. Commercial Pt/C (20 wt.% metal) was purchased from Shanghai Hesen Electric Co., Ltd.

All chemicals (including solvents) were analytical grade and used without further purification unless otherwise noted. The water used in all experiments was deionized (DI) water.

Preparation of Pt-Ni/CNT-o

The Pt-Ni heterojunction samples were prepared by galvanic replacement. Specifically, 1g nickel-plated carbon nanotubes (Ni/CNT) are dispersed in 10 ml H_2O and heated to a boil under stirring. Then 3ml H_2PtCl_6 solution (1 g/ml) was added to the above mixture by drops and kept boiling for 10 min. After cooling to room temperature, the precipitate was centrifuged and washed several times with saturated KCl solution. Finally, drying overnight vacuum at 70℃, the black powder was obtained, which was recorded as Pt-Ni/CNT-o.

Preparation of Pt-Ni/CNT-p

The Pt-Ni/CNT-o sample was then transferred to a porcelain boat and annealed at 200 °C for 2 h with a heating rate of 3 °C min^{-1} in H_2/Ar (5%/95%, 50 ml min^{-1}) atmosphere. Finally, black powders were obtained after grinding manually, denoted as Pt-Ni/CNT-p. The Pt mass loading of Pt-Ni/CNT-p sample was about 5.88 wt% measured by ICP characterization.

Preparation of Pt-Ni/CNT-r

The synthesis process of *Pt-Ni/CNT-r* is the same as that of Pt-Ni/CNT-p, but with infusion of Fe^{3+} solution for 1 h and the final products are correspondingly named as *Pt-Ni/CNT -r*.

Characterizations

XRD patterns were measured at room temperature on a Bruker D8 Advance Powder Diffractometer with Cu Kα radiation (scanning range 10-80°, scanning speed 5°/min, working voltage 40 kV). The scanning electron microscopy (SEM, Zeiss Supra 55) operated at 10 kV was used to characterize the morphology and structure of all samples. TEM images of samples were obtained from a JEM 1200EX transmission electron microscope (JEOL, Japan) operated at 100 kV. The high-resolution TEM (HRTEM), high-angle annular dark-field scanning TEM (HAADF-STEM) and energy dispersive X-ray (EDX) mapping images were acquired with a JEM-2100F field emission electron microscope (JEOL, Japan) operating at an accelerating voltage of 200 kV. A Kratos AXIS Ultra DLD system with Al Kα radiation as the X-ray source was performed to obtain the XPS information. The Pt amount of Pt-Ni/CNT-p, were analyzed by inductively coupled plasma optical emission spectrometry (HORIBA Jobin Yvon, Ultima2). The binding energies calibration was referenced the main peak of the C 1*s* at 284.8 eV. O_2 temperature-programmed desorption (O_2-TPD) curves were measured on a Micromeritics Autochem II 2920 instrument. The concentration of desorbed O_2 was determined by a thermal conductivity cell detector over atemperature rise range of 50-500 °C.

Electrochemical Measurements

All electrochemical tests were carried out on an electrochemical workstation (CHI 760E) with a standard three-electrode system under the 0.1 M KOH solution and room temperature (25 °C). A graphite rod and Hg/HgO electrode were applied as the counter electrode and reference electrode, respectively. The glassy carbon electrode loading catalyst inks were performed as the working electrode. To prepare the catalyst ink, 5 mg of the sample was dispersed in a solution containing 500 μL 0.5 w

t.% Nafion and 500 μL ethanol, and then the ink was dispersed by ultrasound for at least 30 minutes. After that, 10 μL solution was dropped at the glassy carbon electrode (0.196 cm^{-2} for the active geometric area) and dried in room temperature. The catalyst loading of Pt-Ni/CNT-p on the glassy carbon electrode was 0.25 mg cm^{-2}. As a comparison, the x control sample and Pt/C electrodes were also measured. As for HOR experiments, linear sweep voltammetry (LSV) was tested with sweep rates of 5 mV s^{-1} at various rotation rates from 400 rpm to 1600 rpm in the H_2-saturated electrolytes. *i*R compensation was applied to all initial data except stability data. All the potential values were calculated according to the equation, $E_{RHE} = E_{Hg/HgO} + E^{o}_{Hg/HgO} + 0.059$ pH. (1)

The kinetic current (j_k) was calculated according to the Koutecky–Levich equation:

$$\frac{1}{j_g} = \frac{1}{j_k} + \frac{1}{j_d} = \frac{1}{j_k} + \frac{1}{Bc_0\omega^{\frac{1}{2}}} \quad (2)$$

where j_g is the measured geometrical current density and j_d represents the diffusion current density. The j_d can be calculated by the Nernstian diffusion equation:

$$\eta_{diffusion} = -\frac{RT}{2F}\left(1 - \frac{j_d}{j_l}\right) \quad (3)$$

Where $\eta_{diffusion}$ is the over-potential of the electrode, R is the ideal gas constant (8.314 $J \cdot mol^{-1} \cdot K^{-1}$), T is the temperature (in Kelvin). F is the Faraday constant (96485 C mol^{-1}), j_l is the diffusion limiting current, which can be described by Levich equation.

$$j_l = 0.62nFAD^{2/3}\nu^{-1/6}c_0\omega^{1/2} \quad (4)$$

Where n is the number of transferred electrons of the reaction, A is the geometric area of the electrode, D is the H_2 diffusion constant in the electrolyte, $c0$ is the concentration of H_2, ω is the rotation speed of the electrode, and ν is the kinetic viscosity. If a catalyst was assessed in H_2-saturated 0.1 M KOH at a rotation rate of 1600 rpm, the theoretical j_l is 2.71 mA cm^{-2}.

The exchange current density (j_0) was acquired by fitting j_k with the Butler–Volmer equation:

$$j_k = j_0\left[e^{\frac{\alpha F}{RT}\eta} - e^{\frac{-(1-\alpha)F}{RT}\eta}\right] \quad (5)$$

where R is the universal gas constant (8.314 J mol^{-1} K^{-1}), F is the Faraday constant (96,485 C mol^{-1}), α is the transfer coefficient and T is the temperature (298.15 K).

In a small potential window of the micro-polarization region near the equilibrium potential, j_k approximately equals j_g. In this case, the Butler–Volmer equation can be spread by Taylor's formula and simplified as equation:

$$j_g = j_0\frac{\eta F}{RT} \quad (6)$$

Alternatively, by linearly fitting the polarization curve in the micro-polarization region, the j_0 can also be obtained.

The EIS was measured at different overpotentials with an amplitude voltage of 5 mV in a frequency range of 100 kHz to 100 mHz.

Computational Details

All the calculations are performed in the framework of the density functional theory with the projector augmented plane-wave method, as implemented in the Vienna ab initio simulation package. Spin polarization was also included. The generalzied gradient approximation (GGA) proposed by Perdew, Burke, and Ernzerhof is selected for the exchange-correlation potential. A DFT-D3 scheme of dispersion correction was used to describe the van der Waals (vdW) interactions in molecule adsorption. The cut-off energy for plane wave is set to 450 eV. The energy criterion is set to 1E-05 eV in iterative solution of the Kohn-Sham equation. All the structures are relaxed until the residual forces on the atoms have declined to less than 0.02 eV/Å. The electron smearing width of σ = 0.03 eV was employed according to the Gaussian smearing technique. The Brillouin zone integration is performed using

the uniformly distributed scattering of going through the Gamma point to select a 2x1x1 k-mesh in the Monkhorst-Pack grid to make structure optimization.

The pathway by which the HOR occurs under base condition are generally reported to proceed according to the following step:

$$* + 1/2H_2 \rightarrow *H$$

$$*H + OH^- \rightarrow *H + OH* + e^-$$

$$*H + OH* \rightarrow * + H_2O$$

Where the * refers to the catalytic, and the *one refers to the species that adsorbed on the activity sites.

Neglect PV contribution to translation for adsorbed molecules, the free energy was calculated according to the equation of $G = E + H_{cor} – TS = E + G_{cor}$, where E is the energy of every specie obtained from DFT calculations, and S are entropy, while T is 298.15 K. The H_{cor} and G_{cor} are the thermal correction to enthalpy and the thermal correction to Gibbs free energy, respectively. These G_{cor} of intermediate* were taken from the frequency DFT calculation and got value by using Vaspkit.1.4.. The Gibbs free energy of the proton-electron pairs related in the PECT progress, whereas the fact that the proton-electron pairs is in equilibrium with gaseous H_2: $G(H^+ + e^-) = 1/2\ G(H_2$ (g)). According to Vaspkit.1.4.1, the internal energy of gas molecular gained from the formula: $U(T) = ZPE + \Delta U(0\text{-}T)$, the enthalpy of gas molecular gained from the formula: $H(T) = U(T) + PV = ZPE + \Delta U(0\text{-}T) + PV$, and the Gibbs free energy of gas molecular gained from the formula: $G(T) = H(T) - TS = ZPE + \Delta U(0\text{-}T) + PV – TS =$ E_DFT + G cor'. Where E_DFT is the energy of the free gas molecule obtained from DFT calculations, G_cor' is the thermal correction to Gibbs free energy of the free gas molecule obtained from the frequency DFT calculation and got value by using Vaspkit.1.4.1, with the temperature of 298.15K, the pressure of H_2(g) and H_2O(l) were 1atm and 0.035 bar, and all input 1 as the value of spin multiplicity.

Supporting Figures

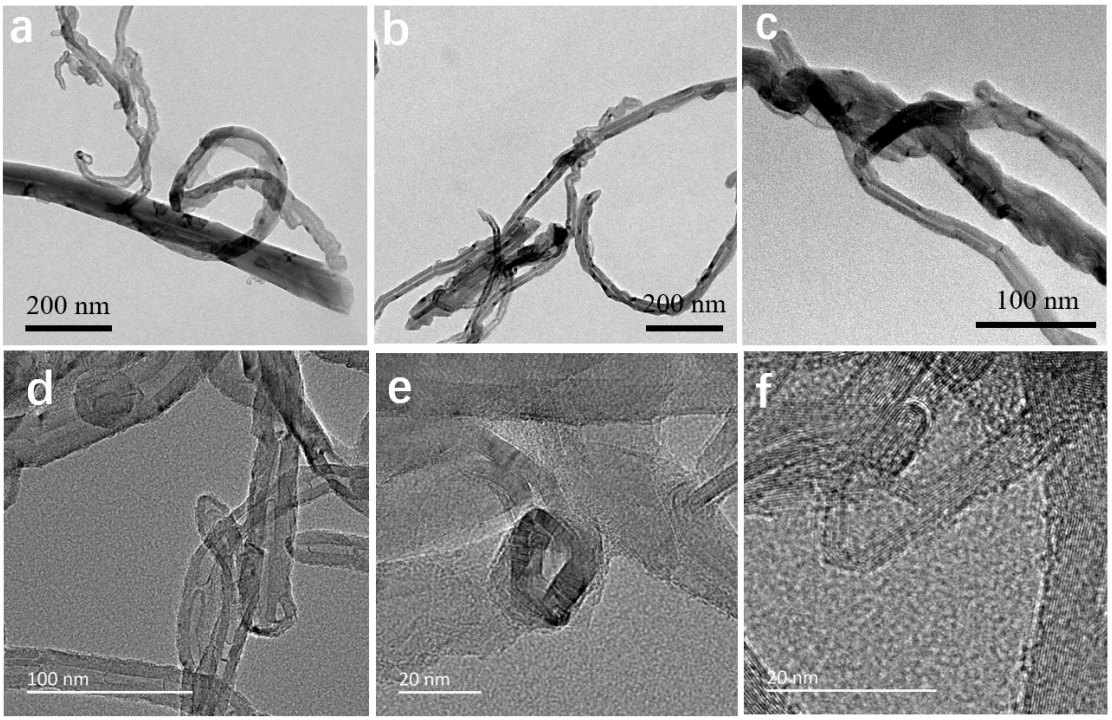

Fig. S1. Typical TEM images of Ni/CNT. (a-d) low resolution images. (e,f) high-resolution image with local magnification.

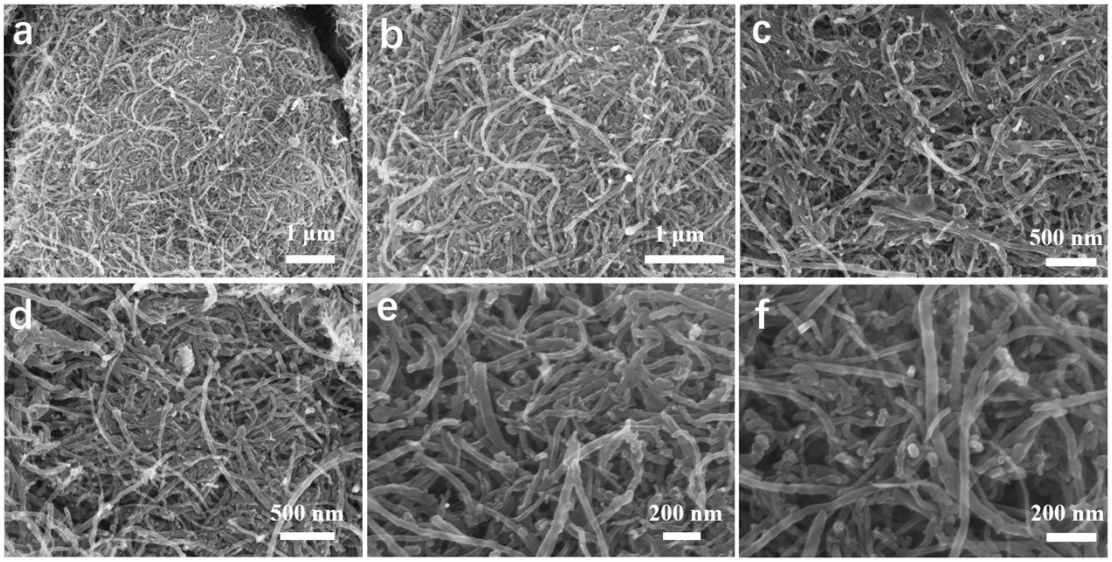

Fig. S2. Typical SEM images of Pt-Ni/CNT-p. (a-c) low resolution images. (d-f) high-resolution image with local magnification.

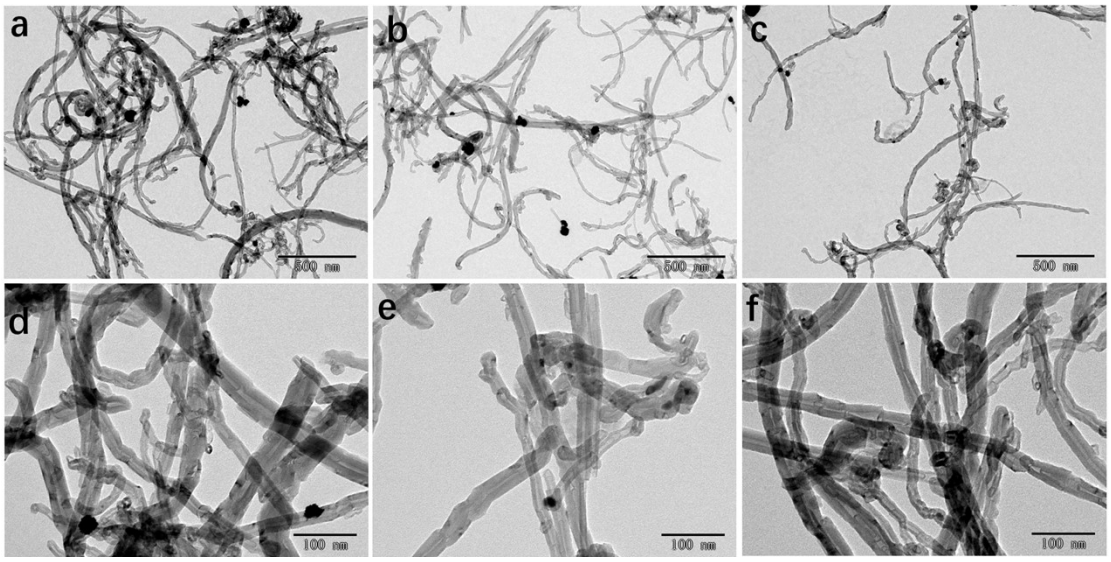

Fig. S3. Typical TEM images of Pt-Ni/CNT-p. (**a-d**) low resolution images. (**e, f**) high-resolution image with local magnification.

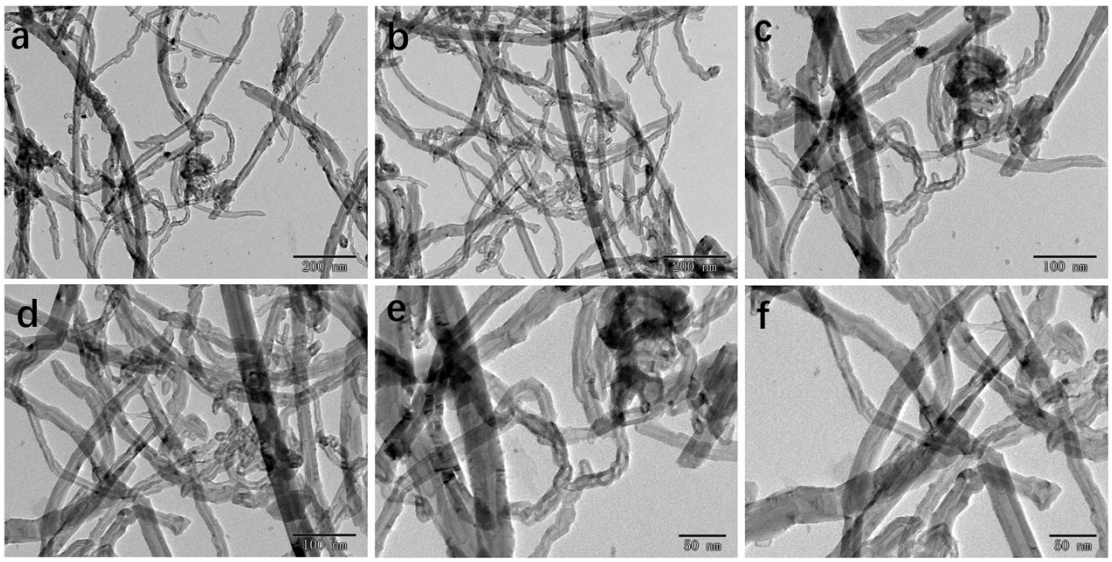

Fig. S4. Typical TEM images of Pt-Ni/CNT-o. (**a-d**) low resolution images. (**e,f**) high-resolution image with local magnification.

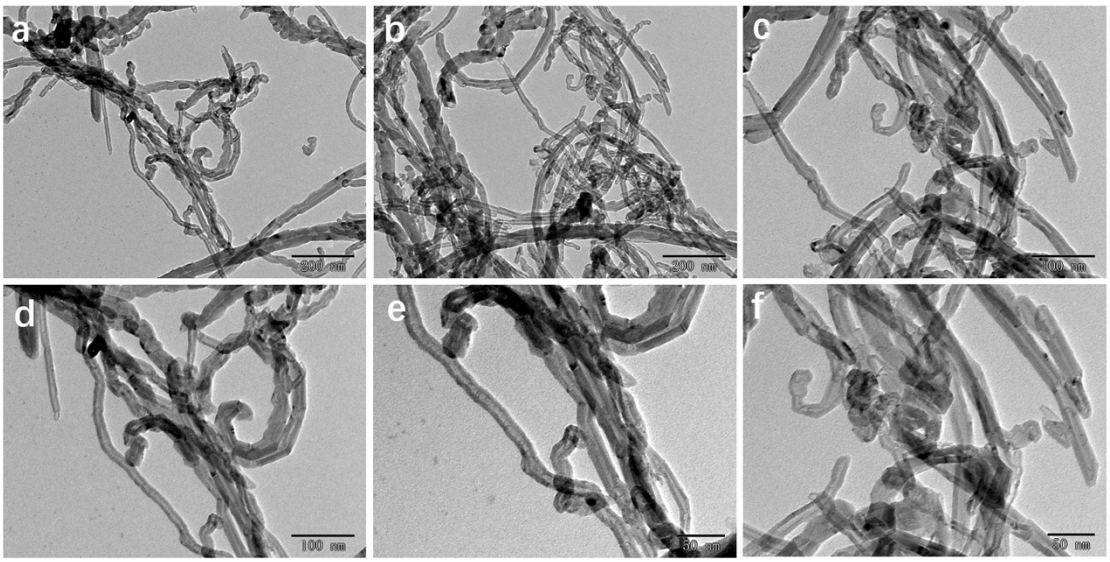

Fig. S5. Typical TEM images of Pt-Ni/CNT-r. (**a-d**) low resolution images. (**e,f**) high-resolution image with local magnification.

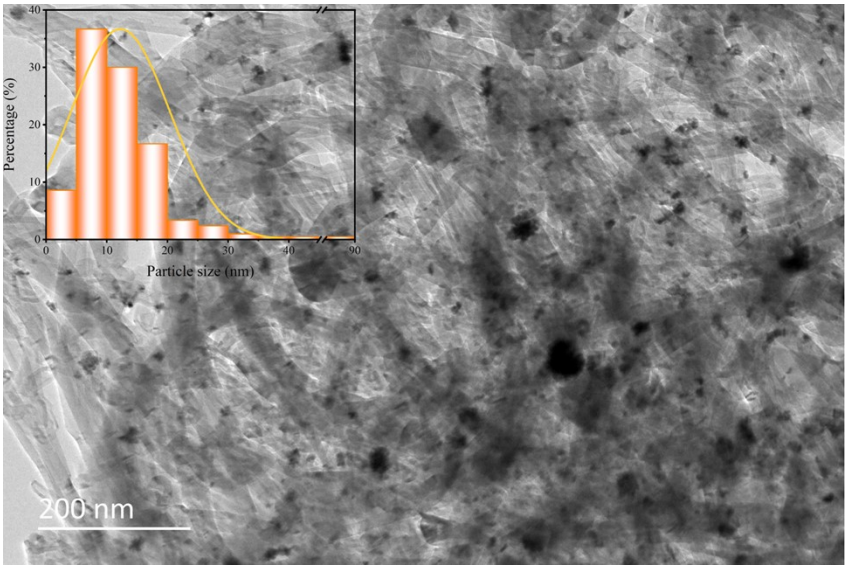

Fig. S6. TEM image of Pt-Ni/CNT-p (inset: particle size distribution).

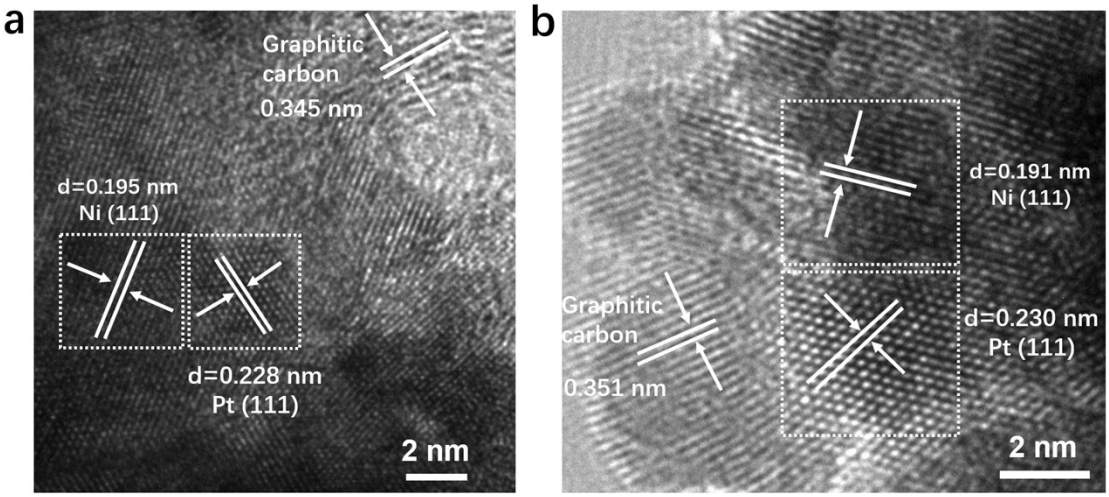

Fig. S7. High-resolution TEM image of the Pt-Ni interface. (a) Pt-Ni/CNT-o. **(b)** Pt-Ni/CNT-r.

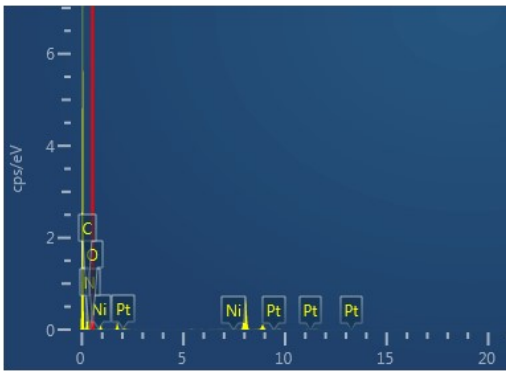

Fig. S8. The corresponding EDS spectra of C, O, Pt, Ni element for Pt-Ni/CNT-p catalyst.

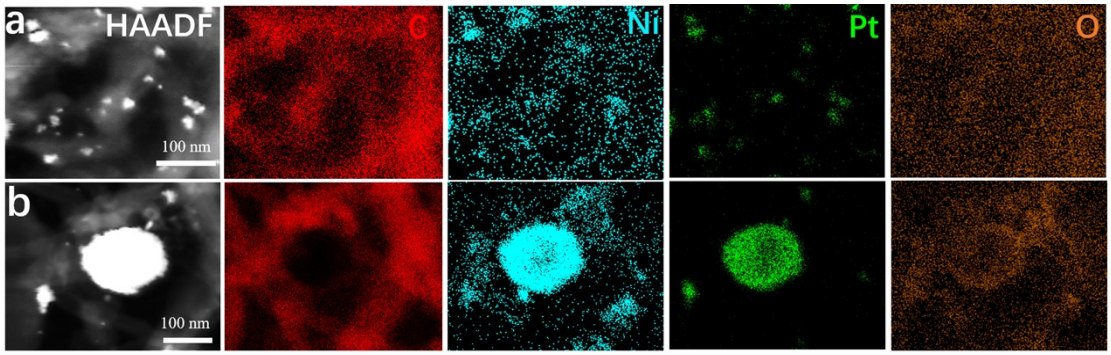

Fig. S9. HAADF-STEM images of Pt-Ni/CNT-p, and the corresponding EDS element mapping distributions of C, Ni, Pt, O.

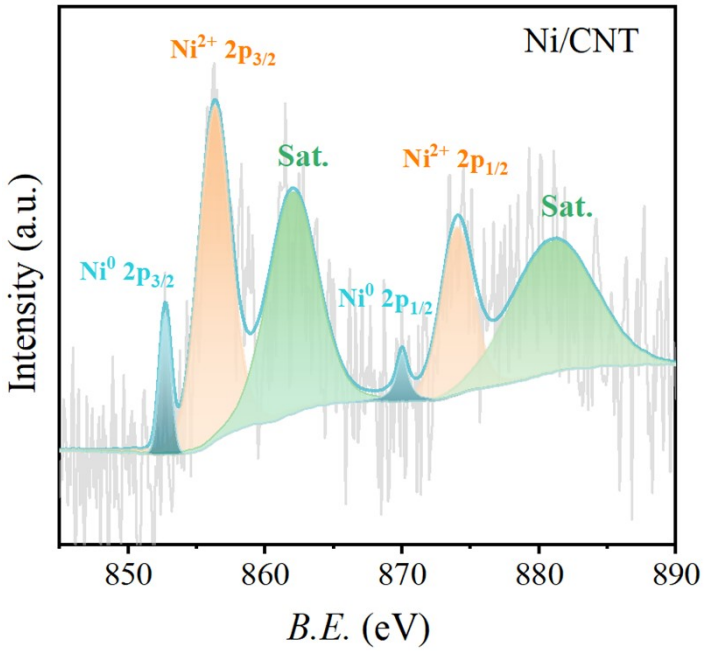

Fig. S10 High-resolution Ni 2p XPS spectra for Ni/CNT.

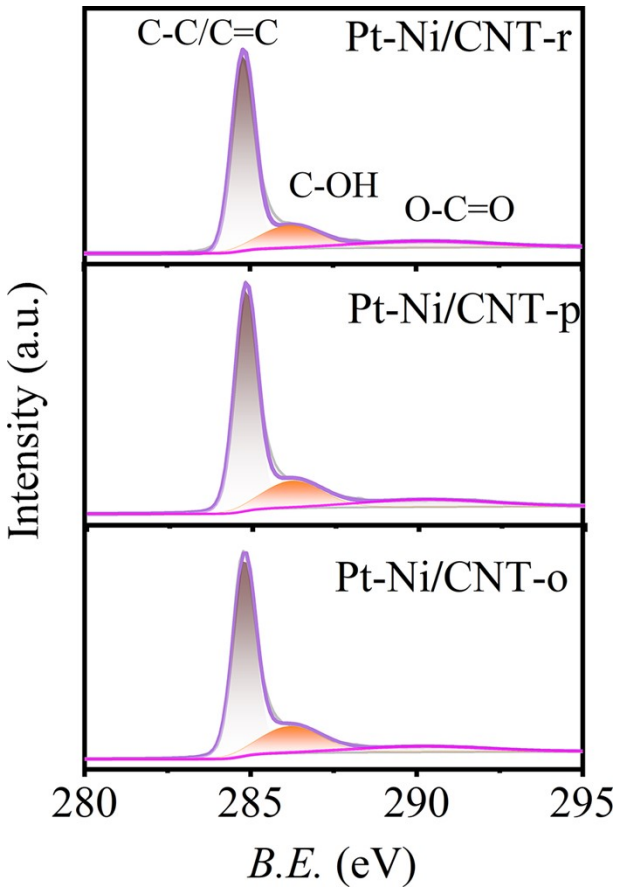

Fig. S11. High-resolution C 1s XPS spectra for Pt-Ni/CNT-p and contrast samples.

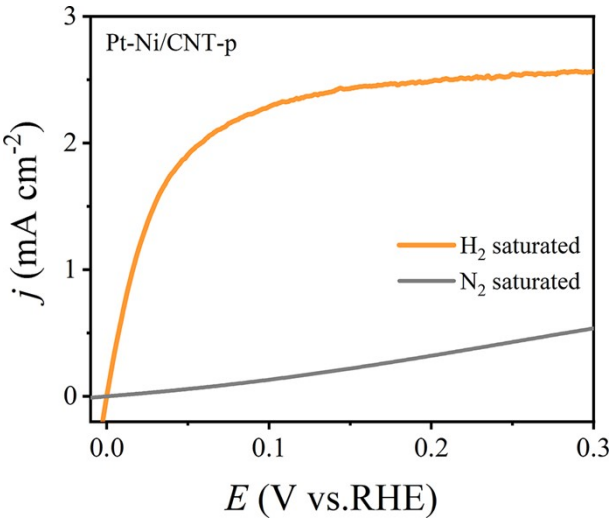

Fig. S12. The HOR comparative test for Pt-Ni/CNT-p catalysts. Comparison of HOR polarization curves in N_2 and H_2 atmospheres.

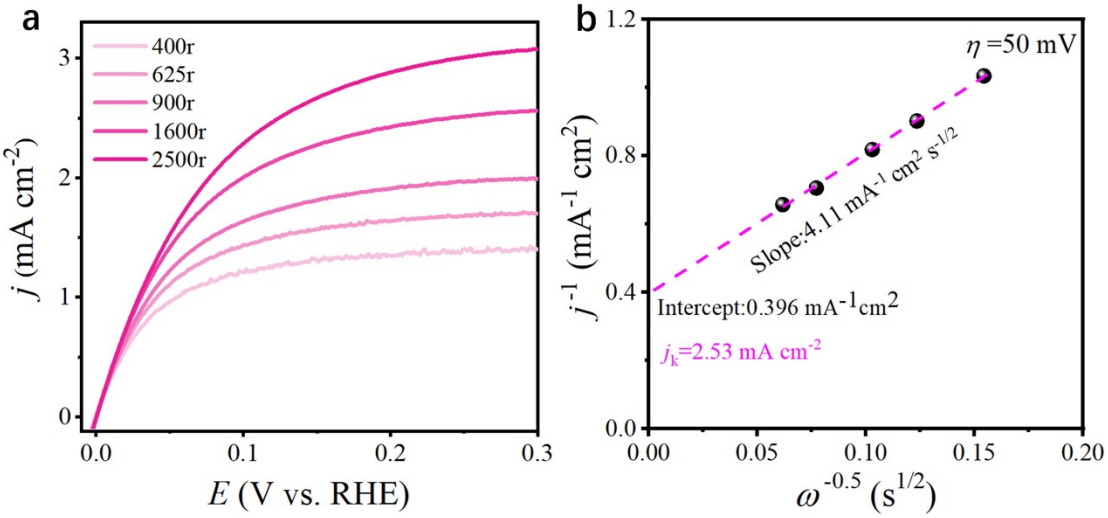

Fig. S13. Alkaline HOR performance for commercial Pt/C. (**a**) polarization curves recorded at various rotation speeds. (**b**) *K-L* plot of corresponding speed at η=50 mV.

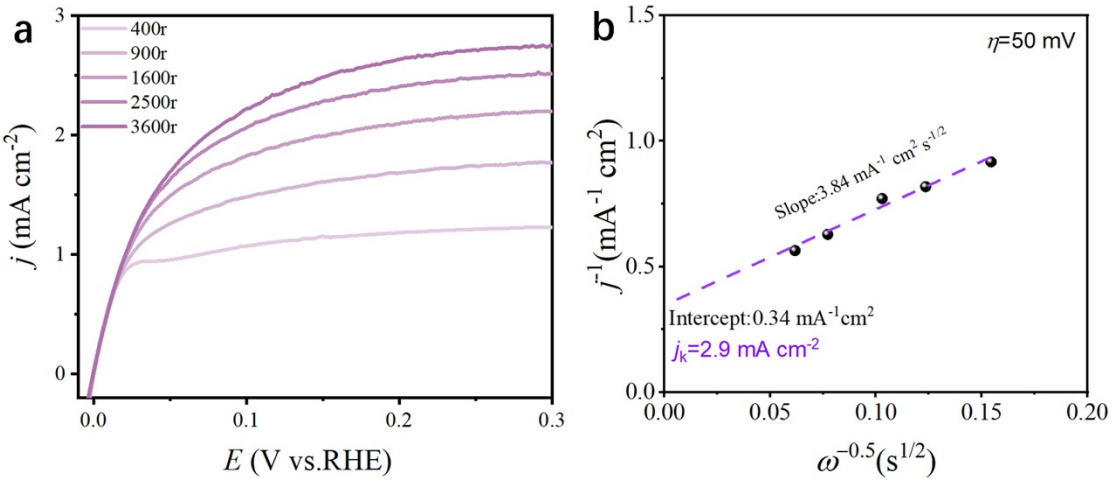

Fig. S14. Alkaline HOR performance for Pt-Ni/CNT-o catalyst. (**a**) polarization curves recorded at various rotation speeds. (**b**) *K-L* plot of corresponding speed at η=50 mV.

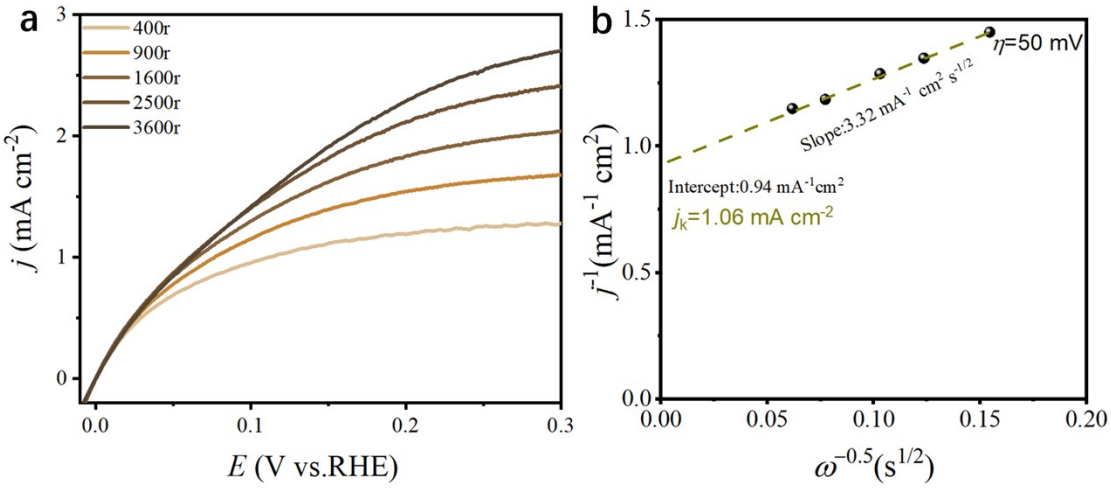

Fig. S15. Alkaline HOR performance for Pt-Ni/CNT-r catalyst. (**a**) polarization curves recorded at various rotation speeds. (**b**) *K-L* plot of corresponding speed at η=50 mV.

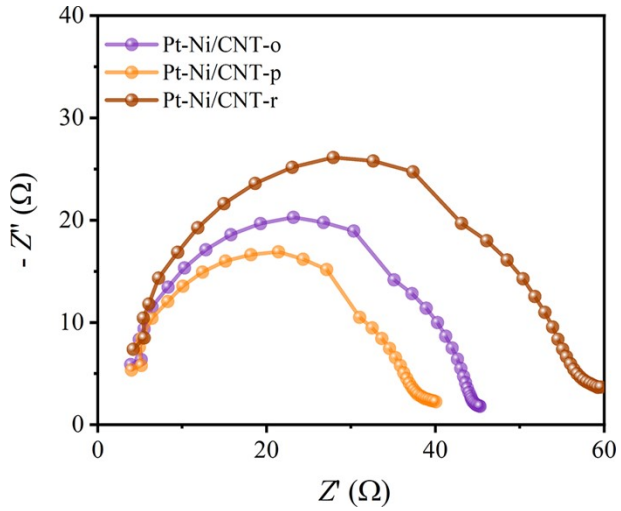

Fig. S16. Electrochemical Impedance Spectroscopy (EIS) of Pt-Ni/CNT-x (x=o, p, r).

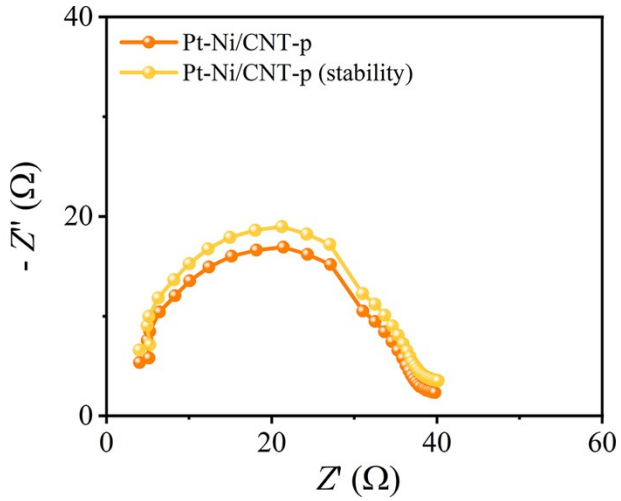

Fig. S17. Electrochemical Impedance Spectroscopy (EIS) of Pt-Ni/CNT-p before and after the HOR electrolysis stability.

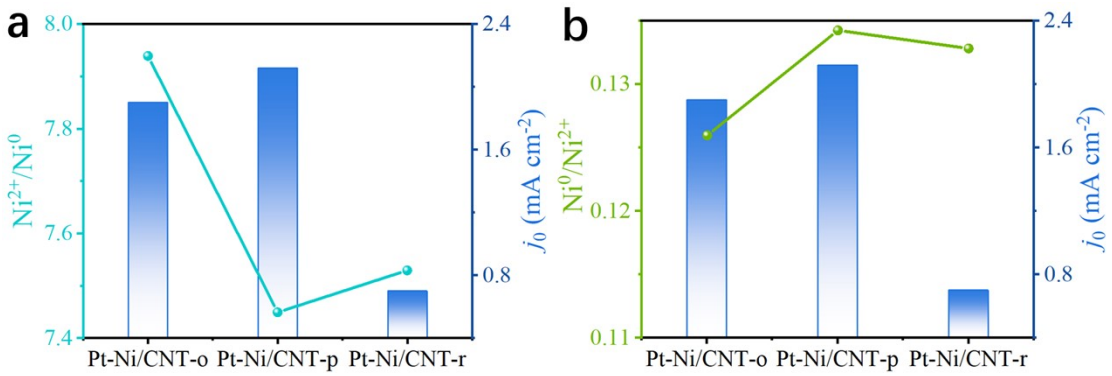

Fig. S18. The plots of different integral area percentage of (a) Ni^{2+}/Ni^{0} and **(b)** Ni^{0}/Ni^{2+} with respect to j_0 for different Pt-Ni/CNT-x (x=o, p, r) electrocatalysts.

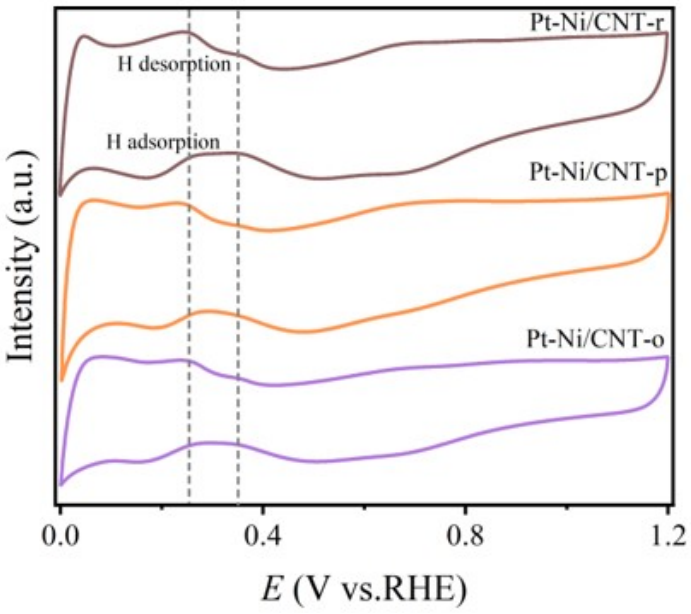

Fig. S19. CV curves recorded in a N_2-saturated 0.1 M KOH solution.

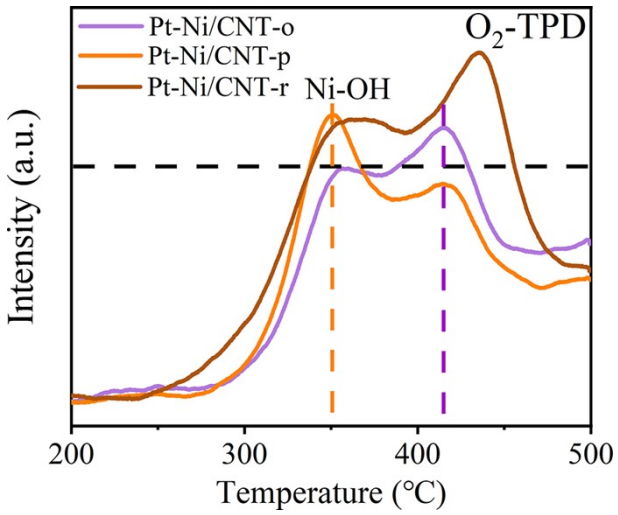

Fig. S20. O_2-TPD spectra of Pt-Ni/CNT-x (x=o, p, r) samples.

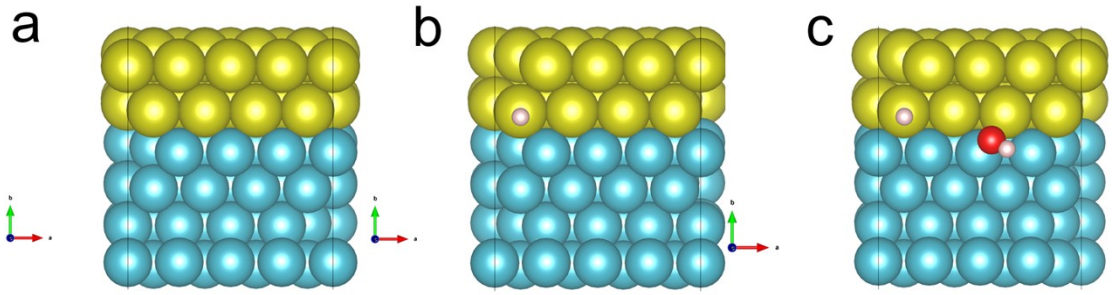

Fig. S21. Optimized configurations of the (a) Pt-Ni-zero interface model with exposed (111) surface; **(b)** H* adsorb model with exposed interface; **(c)** H* and OH* co-adsorb model with exposed interface. (The yellow, cyan, pale pink and red models represent the Pt, Ni, H and O atoms, respectively, as below)

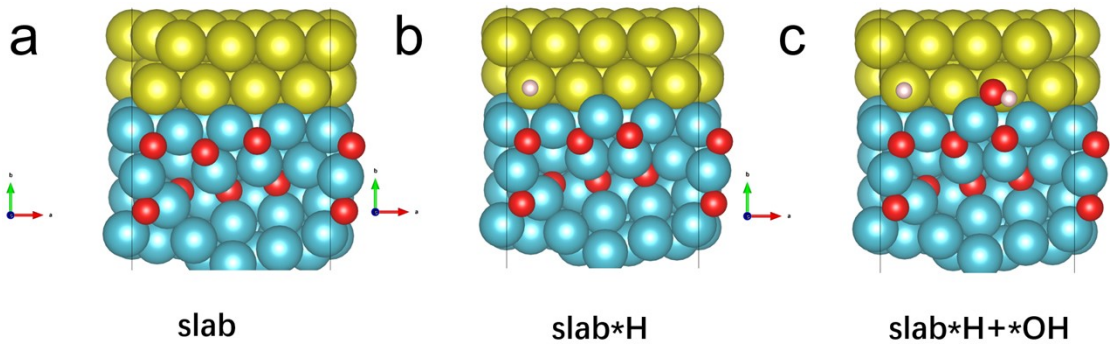

Fig. S22. Optimized configurations of the (a) Pt-NiO_x-middle interface model with exposed (111) surface; **(b)** H* adsorb model with exposed interface; **(c)** H* and OH* co-adsorb model with exposed interface.

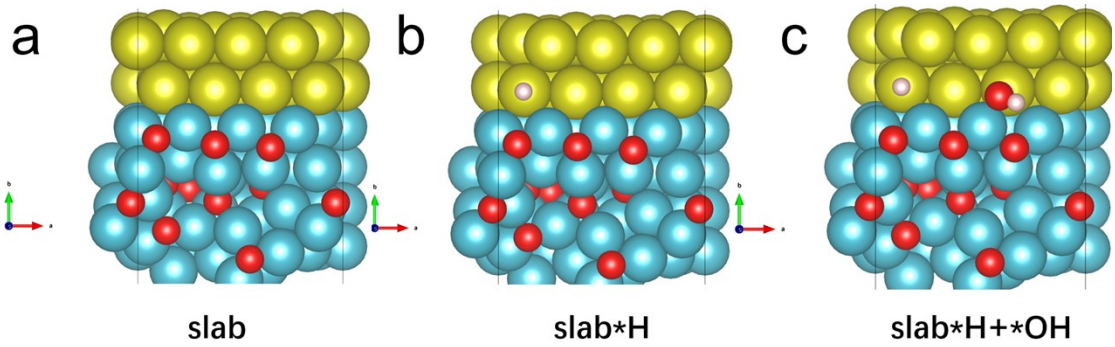

Fig. S23. Optimized configurations of the (a) Pt-NiO_x-excess interface model with exposed (111) surface; **(b)** H* adsorb model with exposed interface; **(c)** H* and OH* co-adsorb model with exposed interface.

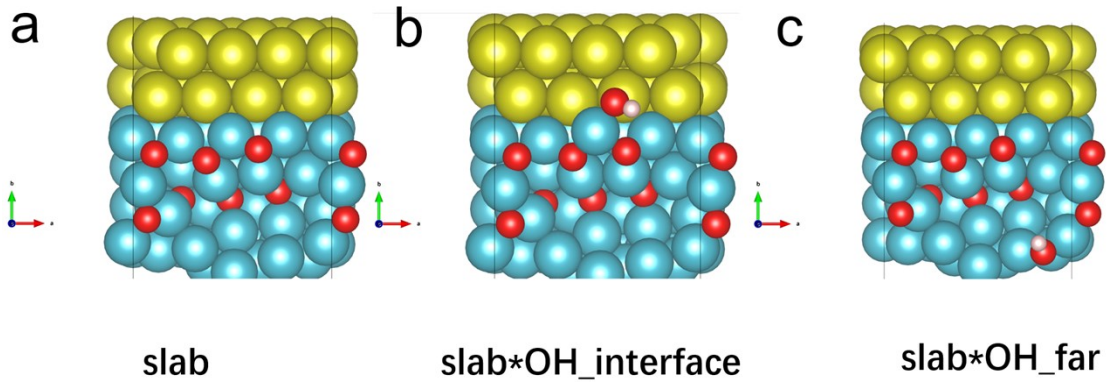

Fig. S24. Different adsorption sites for OH* intermediates in Pt-NiO_x-middle model. (a) Pt-NiO_x-middle interface model with exposed (111) surface; **(b)** OH* adsorb model with exposed interface; **(c)** OH* adsorb model with exposed far.

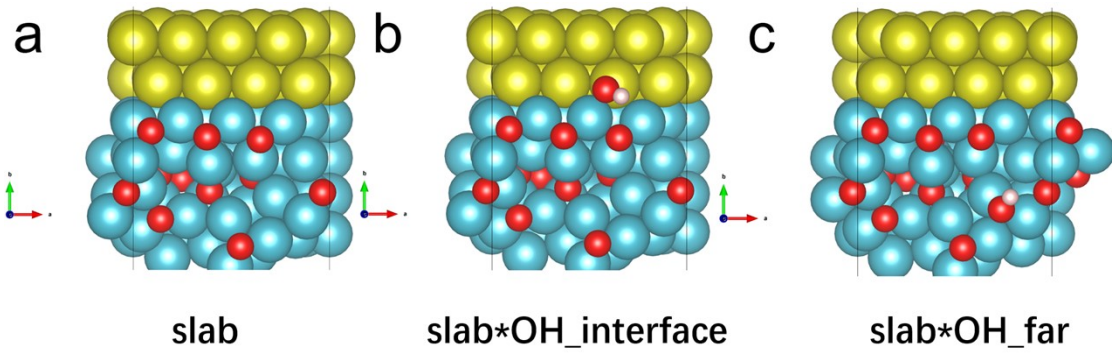

Fig. S25. Different adsorption sites for OH* intermediates in Pt-NiO_x-excess model. (a) Pt-NiO_x-excess interface model with exposed (111) surface; **(b)** OH* adsorb model with exposed interface; **(c)** OH* adsorb model with exposed far.

Table S1. Reduction potential of metal with respect to a standard hydrogen electrode (SHE).

Reduction reaction	E^0 (V vs. SHE)
$Fe^{3+} + e^- \rightarrow Fe^{2+}$	0.77
$Ni^{2+} + 2e^- \rightarrow Ni^0$	-0.25
$Pt^{2+} + 2e^- \rightarrow Pt^0$	1.18

Table S2. The content of Fe species in Pt-Ni/CNT-r obtained from ICP results.

Smaple	Fe (wt%)
Pt-Ni/CNT-r	0.26

Sample	O content (%)
Pt-Ni/CNT-o	7.61
Pt-Ni/CNT-p	6.29
Pt-Ni/CNT-r	7.34

Table S3. Oxygen content is shown in O 1s high-resolution XPS spectra.

Table S4. Summary of the j_0 and transfer coefficients (α) of Pt-Ni/CNT-x and commercial Pt/C.

Electrocatalysts	j_0 (mA cm^{-2})		α
	Butler-Volmer fitting	Micro-polarization	
Pt-Ni/CNT-o	1.90	1.92	0.50
Pt-Ni/CNT-p	2.12	2.11	0.50
Pt-Ni/CNT-r	0.70	0.80	0.60
Pt/C	1.24	1.10	0.50

According to the previous studies (refs. S1 and S3), the obtained α values fall into around 0.5, indicative of a good symmetry for the HOR and HER branches.

Table S5. Comparison of HOR activities and the relevant parameters of the previously reported catalysts in alkaline media.

	Electrocatalysts	$j_{g@0.05\ V}$ (vs. RHE) [a]	j_0	$j_{m,k,0.05V}$ (vs. RHE)	Stability	CO tolerance	Reference
Noble-free electrocatalysts	Ni/N-CNT	~ [b] 1.2 mA cm^{-2}	0.028 mA cm^{-2}_{Ni}	9.3 A g^{-1}_{Ni}	– [c]	–	*Nat. Commun.* 2016, *7,* 10141.
	Ni-CNT	–	0.0092 mA cm^{-2}_{Ni}	1.9 A g^{-1}_{Ni}	–	–	
	Ni	–	0.013 mA cm^{-2}_{Ni}	0.28 A g^{-1}_{Ni}	–	–	
	np-Ni_3N	1.7 mA cm^{-2}	10.3 mA mg^{-1}_{Ni}	29.8 A g^{-1}_{Ni}	12,000 s	~100 s (50,000 ppm CO)	*Energy Environ. Sci.* 2019, *12*, 3522.
	Ni/NiO/C-700	~ 0.9 mA cm^{-2}	0.026 mA cm^{-2}_{Ni}	5.0 A g^{-1}_{Ni}	14,400 s	28,800 s (100 ppm CO, ~70%)	*Angew. Chem.* 2019, *131*, 10754.
	Ni_3N/C	~1.6 mA cm^{-2}	0.014 mA cm^{-2}_{cat}	24.38 A g^{-1}_{Ni}	5,000 CV	–	*Angew. Chem. Int. Ed.* 2019, *58*, 7445.
	Ni_3N	–	0.017 mA cm^{-2}_{cat}	1.73 A g^{-1}_{Ni}	–	–	
	CeO_2(r)-Ni/C-1	~ 1.1 mA cm^{-2}	0.038 mA cm^{-2}_{Ni}	12.28 A g^{-1}_{Ni}	1,000 CV	–	*Angew. Chem. Int. Ed. 2019, 131, 14317.*
	CeO_2-Ni/C-1	–	0.026 mA cm^{-2}_{Ni}	8.48 A g^{-1}_{Ni}	–	–	
	Ni/C	–	0.016 mA cm^{-2}_{Ni}	5.89 A g^{-1}_{Ni}	–	–	
	Ni@O_i-Ni	~2.1 mA cm^{-2}	0.071 mA cm^{-2}_{Ni}	85.63 A g^{-1}_{Ni}	2,000 CVs (89%)	3,600 s (100 ppm CO, 82.3%)	*J. Am. Chem. Soc*., 2022, 144, 12661
	Ni@O_i^d-Ni	~1.5 mA cm^{-2}	0.036 mA cm^{-2}_{Ni}	23.41 A g^{-1}_{Ni}	–	3,600 s (100 ppm CO, 60.5%)	
	Ni@O_i^r-Ni	~2.0 mA cm^{-2}	0.047 mA cm^{-2}_{Ni}	38.57 A g^{-1}_{Ni}	–	3,600 s (100 ppm CO, 65.6%)	
	Ni-H_2-NH_3	~2.3 mA cm^{-2}	0.07 mA cm^{-2}_{Ni}	59.2 A g^{-1}_{Ni}	1,000 CVs (82%)	(7.5% CO, ~66%)	*Nat. Mater.,* 2022, 21, 804.
	Ni-NH_3	–	0.02 mA cm^{-2}_{Ni}	12.7 A g^{-1}_{Ni}	–	–	
	Ni-H_2	–	0.018 mA cm^{-2}_{Ni}	0.8 A g^{-1}_{Ni}	–	–	
	4.3%N–Ni	~2.5 mA cm^{-2} (1 mV s^{-1})	0.041 mA cm^{-2}_{Ni}	77.13 A g^{-1}_{Ni}	21,600 s / 2,000 CVs	(1,000 ppm CO, 96.4%)	*Energy Environ. Sci*., 2022, 15, 1234
	3.5%N–Ni	~2.2 mA cm^{-2} (1 mV s^{-1})	0.035 mA cm^{-2}_{Ni}	30.85 A g^{-1}_{Ni} [d]	–	–	
	1.6%N–Ni	~1.9 mA cm^{-2}	0.029 mA cm^{-2}_{Ni}	18.81 A g^{-1}_{Ni} [d]	–	–	

	Electrocatalysts	(1 mV s^{-1}) $j_{g@0.05\ V}$ (vs. RHE) [a]	j_0	$j_{m,k,0.05V}$ (vs. RHE)	Stability	CO tolerance	Reference
Noble electrocatalysts	Ir/Ni-NiO/CNT	2.5 mA cm^{-2}	2.04 mA cm^{-2}	1590 A g_{Ir}^{-1}	1,000 CVs	–	*J. Mater. Chem. A, 2023, **11**, 5076*
	Ir_2Ni_8/NHCSs	1.5 mA cm^{-2}	2.46 mA cm^{-2}	540 A g_{Ir}^{-1}	5,000 s / 1,000 CVs	–	*Fuel, 2022, **319**, 123637.*
	Ni-Ir(BCS)/G	2.1 mA cm^{-2}	2.97 mA cm^{-2}	330 A g_{Ir}^{-1}	**1**15,000 s (88.1%)	4000 s (1000 ppm CO, 79.6%)	*J. Am. Chem. Soc.*, 2023, **145**, 13805.
	Ni@IrNi	2.2 mA cm^{-2}	2.38 mA cm^{-2}	2340 A g_{Ir}^{-1}	6,000 s (~100%)	–	*Energy Environ. Sci., 2023, **16**, 6120*
	IrNi	–	–	188 A g_{Ir}^{-1}	–	–	*Nanoscale* 2018, *10,* 4872.
	IrNi@PdIr	~2.02 mA cm^{-2}	2.12 mA cm^{-2}	854 A g_{PGM}^{-1}	2,000 CVs (94.9%)	–	
	IrNi@Ir	~2.1 mA cm^{-2}	1.22 mA cm^{-2}	1120 A g_{Ir}^{-1}	1,000 CVs (97.3%)	–	*Nano Energy* 2019, *59,* 26.
	RuNi/NC	~2.01mA cm^{-2}	2.69 mA cm^{-2}	132.6 A g_{RuNi}^{-1}	30 h (88%)	2,000 s (200 ppm CO, 90%)	*Sci. Adv., 2022, 8, eabm3779*
	Ru-Ru_2P	–	3.05 mA cm^{-2}	1265 A g_{Ru}^{-1}	1,000 CVs	–	*Angew. Chem., Int. Ed., 2023, 62, 15585*
	$IrWO_x$/C	–	1.34 mA cm^{-2}	2160 A g_{Ir}^{-1}	1,000 CVs	–	*Sci. Bull., 2020, **65**, 1735-1742*
	$Ni_{100}Au_1$/C-P	~1.6 mA cm^{-2}	1.96 mA cm^{-2}	17.9 A g_{Ni}^{-1}	6,000 CVs (93%)	1,800 s (100 ppm CO, 88%)	*Chem. Eng. J., 2023, 464, 142692*
	RuP@RuP_2/C	~2.3 mA cm^{-2}	2.65 mA cm^{-2}	44.9 A g_{Ru}^{-1} (20 mV)	1,000 CVs	–	*Adv. Mater., 2022, **34**, 2204624.*
	IO-$RuTiO_2$/C	–	–	907 A g_{Ru}^{-1}	**1**3,500 s (90.2%)	–	*J. Mater. Chem. A, 2020, **8**, 10168*
	Ru_3Sn_7/C	2.25 mA cm^{-2}	2.05 mA cm^{-2}	658 A g_{Ru}^{-1}	1,000 CVs	(95.9%)	*Small, 2023, **19**, 2207603*
	O-RuNi@C-400	~2.1 mA cm^{-2}	1.56 mA cm^{-2}	601 A g_{Ru}^{-1}	**1**1,200 s (96.2%)	2,000 s (1000 ppm CO, 92%)	*ACS Mater. Lett., 2022, **4**, 2097.*
	Ir/MoS_2	~2.0 mA cm^{-2}	1.28 mA cm_{ECSA}^{-2}	560 A g_{Ir}^{-1}	**1**12,000 s	–	*Adv. Energy Mater., 2023, **13**, 2202913*

				(~85%)			
Electrocatalysts		**$j_{g@0.05\ V}$ (vs. RHE) [a]**	**j_0**	**$j_{m,k,0.05V}$ (vs. RHE)**	**Stability**	**CO tolerance**	**Reference**
	Ru SA/WC_{1-x}	~2.0 mA cm^{-2}	4.0 mA cm^{-2}	876.1 A g_{Ru}^{-1}	3,000 CVs (80%)	–	*Adv. Mater. 2024, 36, 2308899*
	Pt-Ni/CNT-p	1.91 mA cm^{-2}	2.1 mA cm^{-2}	881 A g_{Pt}^{-1}	20 h (91.7%)	3,000 s (1000 ppm CO, 90.2%)	*This Work*
	Pt-Ni/CNT-o	1.76 mA cm^{-2}	1.9 mA cm^{-2}	774 A g_{Pt}^{-1}	–	–	
	Pt-Ni/CNT-r	1.08 mA cm^{-2}	0.7 mA cm^{-2}	294 A g_{Pt}^{-1}	–	–	

[a] Activity obtained at η = 0.05 V vs. RHE. Previous studies have indicated that the kinetic current densities can be measured with reasonable precision in the Tafel region; however, when the polarization curves are approaching the diffusion-controlled overpotential range, there will be large errors to work out the kinetic activity of the catalysts. In this regard, we have chosen the overpotential of 50 mV as a benchmark to compare the alkaline HOR performance of our designed catalysts. Meantime, it should be pointed out that this comparison is widely accepted by other literatures[S1–S3].

[b] All of "~" means that the corresponding parameters are imputed values from the corresponding reference data graph.

[c] All of "−" means that no values were reported for the corresponding parameters in the corresponding references.

[d] The data were calculated from the corresponding references

Table S6. DFT calculation results for Gibbs free energy (G) on various models.

Sites		*G* (eV)
Pt-Ni-zero interface	*	0.00
	H*	-0.29
	H*+OH*	0.58
	*	0.00
Pt-NiO_x-middle interface	*	0.00
	H*	0.55
	H*+OH*	0.81
	*	0.00
Pt-NiO_x-excess interface	*	0.00
	H*	-0.68
	H*+OH*	0.39
	*	0.00

Supplementary references

S1. Ni, W., Wang, T., Schouwink, P., Chuang, Y., Chen, H., Hu, X. Efficient hydrogen oxidation catalyzed by strain-engineered nickel nanoparticles. *Angew. Chem. Int. Ed.* **59**, 10797 (2020).

S2. Yang, F., Bao, X., Li, P., Wang, X., Cheng, G., Chen, S., Luo, W. Boosting hydrogen oxidation activity of Ni in alkaline media through oxygen-vacancy-rich CeO_2/Ni heterostructures. *Angew. Chem.* **131**, 14317 (2019).

S3. Bard, A., Faulkner, L. Electrochemical Methods: Fundamentals and Aplications. (Wiley, 2001).